The Solution Structure of Human Coagulation Factor VIIa in Its Complex with Tissue Factor Is Similar to Free Factor VIIa: A Study of a Heterodimeric Receptor−Ligand Complex by X-ray and Neutron Scattering and Computational Modeling

Alun W. Ashton,[‡] Mark K. Boehm,[‡] Daniel J. D. Johnson,[§] Geoffrey Kemball-Cook,[§] and Stephen J. Perkins*[,‡]

Department of Biochemistry and Molecular Biology, Royal Free Hospital School of Medicine, Rowland Hill Street, London NW3 2PF, U.K., and Haemostasis Research Group, MRC Clinical Sciences Centre, Imperial College Medical School, Hammersmith Hospital, Du Cane Road, London W12 0NN, U.K.

Received October 16, 1997; Revised Manuscript Received March 23, 1998

ABSTRACT: Factor VIIa (FVIIa) is a soluble four-domain plasma serine protease coagulation factor that forms a tight complex with the two extracellular domains of the transmembrane protein tissue factor in the initiating step of blood coagulation. To date, there is no crystal structure for free FVIIa. X-ray and neutron scattering data in solution for free FVIIa and the complex between FVIIa and soluble tissue factor (sTF) had been obtained for comparison with crystal structures of the FVIIa−sTF complex and of free factor IXa (FIXa). The solution structure of free FVIIa as derived from scattering data is consistent with the extended domain arrangement of FVIIa seen in the crystal structure of its complex with sTF, but is incompatible with the bent, less extended domain conformation seen in the FIXa crystal structure. The FVIIa scattering curve is also compatible with a subset of 317 possible extended structures derived from a constrained automated conformational search of 15 625 FVIIa domain models. Thus, the scattering data support extended domain models for FVIIa free in solution. Similar analyses showed that the solution scattering derived and crystal structures of the FVIIa−sTF complex were in good agreement. An automated constrained search for allowed structures for the complex in solution based on scattering curves showed that only a small family of compact models gave good agreement, namely those in which FVIIa and sTF interact closely over a large surface area. The general utility of this approach for structural analysis of heterodimeric complexes in solution is discussed. Analytical ultracentrifugation data and the modeling of these data were consistent with the scattering results. It is concluded that in solution FVIIa has an extended or elongated domain structure, which allows rapid interaction with sTF over a large surface area to form a high-affinity complex.

Inappropriate blood coagulation may result in thrombotic disorders often associated with cardiovascular, infectious, and neoplastic disease. Such coagulation can be initiated by exposure of cell surface expressed tissue factor to plasma. Similar to the full-length transmembrane receptor tissue factor, soluble tissue factor (sTF)[1] forms a high-affinity catalytic enzyme−cofactor complex with the plasma serine protease coagulation factor VIIa (FVIIa), with a dissociation constant K_D estimated by surface plasmon resonance to be in the range 2−5 nM (*1*−*3*). Proteolysis of factor VII to its active form FVIIa proceeds via a cleavage between Arg152 and Ile153. In the presence of Ca^{2+}, this complex catalyzes the conversion of both factor IX to factor IXa (FIXa) and factor X to factor Xa, both of which are active coagulation serine proteases. An understanding of the molecular basis of these initiating procoagulant reactions may in the long term help to treat and even prevent associated thrombotic disorders. Recent reviews give further background to FVIIa and sTF (*4*−*8*).

Both sTF and FVIIa are multidomain proteins (Figure 1). The crystal structure of sTF contains two fibronectin type III domains at an angle of 125° to each other to form an extended but rigid arrangement (*9*−*11*). The domains are identical in structure and topology to C2-type immunoglobulin folds, but exhibit distinct sequence differences (*12*, *13*). FVIIa contains four domains: a serine protease domain (SP), two epidermal growth factor domains (EGF-1 and EGF-2), and a γ-carboxyglutamic acid-rich domain (Gla). The crystal structure of the complex between FVIIa and sTF revealed the location of all four FVIIa domains as well as those for sTF (*14*), but no crystal structure is presently available for free FVIIa. The FVIIa domains are structurally homologous to similar domain structures in activated factors IX and X. Crystal structures of human factor Xa lacking the Gla domain showed the SP and EGF-2 domains, but the EGF-1 domain was not visible for reason of crystallographic disorder and

* To whom correspondence and requests for reprints should be addressed.

[‡] Royal Free Hospital School of Medicine.

[§] Imperial College Medical School.

[1] Abbreviations: FVIIa, factor VIIa; FIXa, factor IXa; sTF, soluble extracellular tissue factor (residues 1−219); SP, serine protease domain; EGF, epidermal growth factor domain; Gla, γ-carboxyglutamic acid-rich domain; R_G, radius of gyration; R_{XS}, radius of gyration of cross section; $R_{2.0}$, *R* factor of agreement.

S0006-2960(97)02574-9 CCC: $15.00
Published on Web 05/08/1998

occupied different positions in the two structures (*15, 16*). That for porcine FIXa showed the SP, EGF-2, and EGF-1 domains and most of the Gla domain (*17*), but there is a striking bend in its domain arrangement in distinction to the linear one seen for FVIIa in its complex with sTF (*14*). Structures for the EGF-1 domains of human factors IX and X and the Gla domain in bovine prothrombin are also available (*18*−*20*). Despite this abundance of homologous atomic structures, little information is available on the domain arrangement free in solution of FVIIa, nor on that of its complex with sTF, nor on the disposition of two large N-linked oligosaccharide chains on FVIIa that were not visible in the crystal structure of the complex (*14*).

Solution scattering provides information on domain arrangements in multidomain proteins (*21, 22*). Recently the usefulness of this technique has been much enhanced by the ability to use either intact crystal structures for scattering curve fitting (*23*−*25*) or individual domain structures in an automated constrained curve-fit procedure (*26*−*28*), both of which result in an improved understanding of the overall structure. Previous X-ray and neutron scattering data for FVIIa, sTF, and their complex in solution correctly predicted the compact nature of the complex between FVIIa and sTF determined by crystallography (*29, 30*). The availability of coordinates for the crystal structures for the FVIIa−sTF complex and for the FVIIa-homologue FIXa now makes possible a quantitative analysis of the FVIIa domain structure in free solution from scattering data, and likewise that for the FVIIa−sTF complex. Knowledge of the domain arrangement of free FVIIa in solution is important for an appreciation of how membrane-bound TF is able to recognize FVIIa as a ligand. A verification of the domain arrangement in solution of the FVIIa−sTF complex provides important confirmation that the crystal structure of the complex is representative of the functional cofactor−enzyme complex. It is also possible to analyze the conformation of the two large N-linked oligosaccharide chains on FVIIa, which are not visible in the crystal structure.

Previous applications of constrained automated scattering curve-fit modeling have determined possible structures of multidomain proteins of unknown structure (*26*−*28*) or of homodimeric and homotrimeric complexes (*25, 31*). This approach is important in cases where it is not possible to derive even a low-resolution structural model for multidomain proteins or their complexes by other methods. The availability of the FVIIa−sTF crystal structure enables the extent to which such a procedure can be applied successfully to a heterodimeric protein−protein complex to be discussed.

METHODS

(a) Crystal Structures Used for Direct Scattering Curve Comparisons. Crystal coordinates for the complex between active-site-inhibited recombinant human FVIIa and subtilisin-cleaved sTF were kindly provided by Dr. D. W. Banner (Brookhaven code 1dan). The domain residue numbering is shown in Figures 1 and 2 (*32*). Two N-linked oligosaccharides at Asn145 in the pre-SP linker and Asn322 in the SP domain (Figure 1) were added as these were not visible in the electron density map, using the modeling package INSIGHT II (Biosym/MSI, San Diego, USA) on Silicon Graphics INDY Workstations. These were constructed as

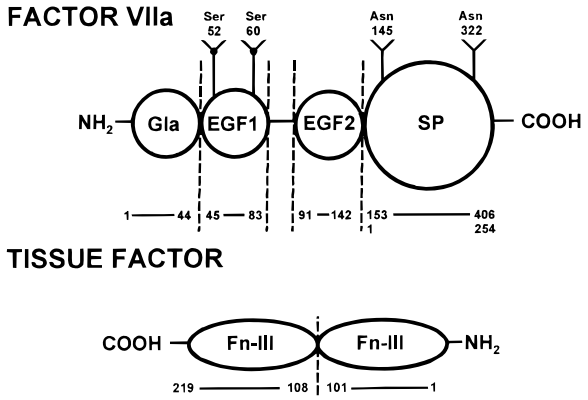

FIGURE 1: Domain structures of human FVIIa and sTF. FVIIa contains an N-terminal Gla domain and two EGF domains in the light chain and a SP domain in the heavy chain. As shown, the membrane-proximal C-terminal domain of sTF is close to the N-terminal Gla domain in FVIIa in the complex. Two O-linked glycosylation sites are found on EGF-1 at Ser52 and Ser60, and two N-linked glycosylation sites are found at Asn145 and Asn322.

the mean biantennary oligosaccharide structure (NeuNAc•-Gal•GlcNAc•Man)$_2$Man•GlcNAc•GlcNAc(Fuc) in FVIIa (*33*), using as a template the nine-residue carbohydrate coordinates of Chain A in the Fc fragment of human IgG1 KOL (1fcl) (*34*). The two O-linked structures in FVIIa were represented by Xyl•Glc at Ser52 and Fuc at Ser60, these being the mean of previously reported structures (*35, 36*). Both O-linked oligosaccharides were modeled from the library of fragments provided by INSIGHT II. Coordinates for the crystal structure of porcine FIXa (1pfx) were adapted to those of human FVIIa by adding two N-linked oligosaccharides at Thr145 and Thr322 and two O-linked oligosaccharides at Pro52 and Leu60 (Figure 2; FVII sequence numbering) in order to replicate the FVIIa oligosaccharide structures. Three sets of human sTF crystal coordinates were used: an initial set for free sTF which was later replaced (1boy) (*9*); a second independent set for free sTF (1hft, replaced after refinement by 2hft) (*10, 11*); and those found in the complex with FVIIa (1dan). While three glycosylation sites occur at Asn11, Asn124, and Asn137 in native sTF, these were not modeled here as the recombinant sTF used for scattering data was expressed in *Escherichia coli* (*37*).

(b) Automated Scattering Curve-Fit Searches for FVIIa and Its Complex with sTF. The automated curve-fit procedure for the FVIIa domains was based on the reconstruction of these domains from available homologous structures which corresponds to the general method used for an unknown multidomain structure (*26*−*29*). The FVIIa residues 1−44 (Figures 1 and 2) were assigned to the Gla domain in prothrombin (code 2pfl) (*20*), residues 45−83 to the EGF-1 domain in factor IX (code 1ixa) (*18, 19*), and residues 91−142 and 153−406 to the EGF-2 and SP domains in factor Xa (code 1hcg) (*15*). This starting model included all 406 residues in FVIIa, except for 7 residues in the link between the two EGF domains and 10 between the EGF-2 and SP domains. The alignment of Figure 2 showed that N-linked oligosaccharide chains were positioned at Arg142 at the C terminus of EGF-2 in factor Xa, and at Ile317 in the SP domain in factor Xa (FVII sequence numbering) to correspond to their locations in FVIIa.

Since the EGF-2 and SP domains form a fixed structure, the starting model for FVIIa curve fits with the *x*-axis, *y*-axis,

```
            1                                                    49
Factor VIIa ANA.FLggLR PGSLgRgCKg gQCSFggARg IFKDAgRTKL FWISYSDGDQ
Prothrombin ANKGFLggVR KGNLgRgCLg gPCSRggAFg ALgSLSATDA FWAKY.....
Factor IXa  YNSGKLggFV RGNLgRgCIg gKCSFggARg VFgNTgKTNg FWKQYVDGDQ
Factor Xa   ANS.FLggMK KGHLgRgCMg gTCSYggARg VFgDSDKTNg FWNKYKDGDQ

            50                                  <.linker.>       99
Factor VIIa CASSPCQNGG SCKDQLQSYI CFCLPAFEGR NCETHKDDQL ICVNENGGCE
Factor IXa  CEPNPCLNGG LCKDDINSYE CWCQVGFEGK NCELDA.... TCNIKNGRCK
Factor Xa   CETSPCQNQG KCKDGLGEYT CTCLEGFEGK NCELFTRK.. LCSLDNGDCD
                                                <.linker.>
            100                                                C 149
Factor VIIa QYCSDHTGTK RSCRCHEGYS LLADGVSCTP TVEYPCGKIP ILEKRNASKP
Factor IXa  QFCKTGADSK VLCSCTTGYR LAPDQKSCKP AVPFPCGRVS VSHSPTTLTR
Factor Xa   QFCHEEQNS. VVCSCARGYT LADNGKACIP TGPYPCGKQT LER.......

            150                                                # 198
Factor VIIa QGRIVGGKVC PKGECPWQVL LLVNGAQ.LC GGTLINTIWV VSAAHCFDKI
Factor IXa  ...IVGGENA KPGQFPWQVL L.NGKIDAFC GGSIINEKWV VTAAHCIEPG
Factor Xa   ...IVGGQEC KDGECPWQAL LINEENEGFC GGTILSEFYI LTAAHCLYQA
                                                               #
            199                                                 # 246
Factor VIIa KNWRNLIAVL GEHDLSEHDG DEQSRRVAQV IIPSTY..VP GTTNHDIALL
Factor IXa  VKIT...VVA GEYNTEETEP TEQRRNVIRA IPHHSYNATV NKYSHDIALL
Factor Xa   KRFK...VRV GDRNTEQEEG GEAVHEVEVV IKHNRF..TK ETYDFDIAVL
                                                                 #
            247                                                  296
Factor VIIa RLHQPVVLTD HVVPLCLPER TFSERTLAFV RFSLVSGWGQ LLDRGATALE
Factor IXa  ELDEPLTLNS YVTPICIADK EYT.NIFLKF GSGYVSGWGR VFNRGRSATI
Factor Xa   RLKTPITFRM NVAPACLPER DWAESTLMTQ KTGIVSGFGR THEKGRQSTR

            297                         C                        #46
Factor VIIa LMVLNVPRLM TQDCLQQSRK VGDSPNITEY MFCAGYSDGS KDSCKGDSGG
Factor IXa  LQYLKVPLVD RATCLRSTKV T.....IYSN MFCAGFHEGG KDSCLGDSGG
Factor Xa   LKMLEVPYVD RNSCKLSSSF I.....ITQN MFCAGYDTKQ EDACQGDSGG
                                                                 #
            347                                                  396
Factor VIIa PHATHYRGTW YLTGIVSWGQ GCATVGHFGV YTRVSQYIEW LQKLMRSEPR
Factor IXa  PHVTEVEGTS FLTGIISWGE ECAVKGKYGI YTKVSRYVNW IKEKTKLT..
Factor Xa   PHVTRFKDTY FVTGIVSWGE GCARKGKYGI YTKVTAFLKW IDRSMKTRGL

            397   406
Factor VIIa PGVLLRAPFP
Factor Xa   PKAK......
```

FIGURE 2: Alignment of the human FVII amino acid sequence with those in bovine prothrombin, porcine FIXa, and human factor Xa to show the sequence identity with structurally homologous domains in the latter. The γ-carboxyglutamic residues in the Gla domain (residues 1−44) are denoted by g, the two N-linked oligosaccharide sites by C, and the catalytic triad (His-Asp-Ser) by #. Underlined sequences correspond to the homology models used for the linear starting model of FVIIa in Figure 5 below. The residue numbering refers to the mature amino acid sequence of human FVIIa.

and *z*-axis rotations set as 0° (see Figure 4 in ref *29*) was created by positioning the N- and C-terminal α-carbon atoms of the Gla, EGF-1, and EGF-2 domains on a long common linear *x* axis with arbitrary separations of 0.5 nm between adjacent N- and C-terminal α-carbon atoms (see Figure 5 below). The origins for the rotational searches were defined as the C-terminal α carbons of Tyr44 (Gla) and Leu83 (EGF-1). The three *y* axes were set to be parallel and were defined arbitrarily by the α-carbon atoms of Lys3 (Gla), Cys81 (EGF-1), and Gly93 (EGF-2). For automated curve fitting (*26*−*28*), rotations to create models were applied to this starting model using a Biosym Command Language (BCL) macro in conjunction with Unix shell scripts. In this, each of the Gla and EGF-1 domains was rotated relative to the EGF-2/SP domain pair into all *x*-, *y*- and *z*-axis orientations, while maintaining a fixed separation between N- and C-termini pairs between adjacent domains. The search utilized five 72° steps on each axis to give 5^6 or 15 625 models.

The curve-fit searches for the complex between FVIIa and sTF used the linear starting model for FVIIa derived from homology modeling and the sTF crystal structure (*9*). The long *x* axis of sTF was defined using the N-terminal α carbon of Thr3 as origin, and the C-terminal α carbon of Glu213. The *y* axis of sTF was defined arbitrarily by the α carbon of Thr86. To initiate the search, the long axis of sTF was aligned parallel to the long axis of the Gla, EGF-1, and EGF-2 domains in the linear starting model for FVIIa. The starting FVIIa and sTF models were superimposed using the sTF and EGF-2 axes in which the common origin was set as the N-terminal α carbon of sTF and the C-terminal α carbon of EGF-2. Then, holding FVIIa fixed in position, sTF was translated from its initial position along the *x*, *y*, and *z* axes in order to generate structures. A total of four 90° reorientations of sTF about its long axis relative to FVIIa were examined in four separate searches in order to investigate the effect of the 125° angle between the two Fn-III domains in sTF on the outcome of the searches. In each search, after an initial translation of sTF of −5 nm on all three axes from the common origin, sTF was translated in 0.5 nm steps from −5 nm to +5 nm along all three axes to give a full range of 21^3 or 9 261 models for each of the four sTF orientations.

(c) Experimental Scattering and Analytical Ultracentrifugation Data. X-ray scattering data from Stations 2.1 and 8.2 at the Synchrotron Radiation Source, Daresbury, and neutron scattering data from the LOQ Instrument at the ISIS facility at the Rutherford-Appleton Laboratory were obtained for active-site-inhibited FVIIa, sTF, and the complex between them (*29*). The full characterization of these samples is described in ref 29 and references therein. Solutions of FVIIa and the FVIIa−sTF complex at 0.2−0.8 mg/mL, prepared as described in ref 29, were analyzed using a Beckman XLA analytical ultracentrifuge operated at 40 000 rpm (An-60 Ti rotor) and equipped with scanning absorption optics at the National Centre for Macromolecular Hydrodynamics, Leicester. Traces were measured at 280 nm and analyzed using a digitizing pad to yield experimental $s^\circ_{20,w}$ values after correction for the density and viscosity of the buffer (*38*).

(d) Modeling of Scattering and Analytical Ultracentrifugation Data. For the direct comparison of scattering curves with crystal structures (Figures 3 and 4 below), sphere models were created by placing each full atomic coordinate set in a three-dimensional grid of cubes of side length 0.370 nm. By varying a cutoff such that a sphere was created at the center of the cube if a given number of atoms were present in the cube, the total volume of the resulting sphere model was set to be equal to the full volume calculated for the 433 and 219 amino acid and carbohydrate residues, respectively, in FVIIa and sTF (*39*). This procedure corrected for any residues that were missing in the crystal structure or altered in homology models based on FIXa or on homologous domains. The FVIIa models contained about 1250 spheres (63.0 nm^3), and those for sTF contained about 630 spheres (31.5 nm^3).

For the comparison of scattering curves from each of the structures calculated from the two automated searches based on homology models (Figures 5 and 6 below), the cube side was increased to 0.452 nm while retaining the same total volume. This reduced the computational resources required for each search. The consistent generation of the sphere models was achieved by fixing both the origin of the grid and the position of the FVIIa model within this grid. The

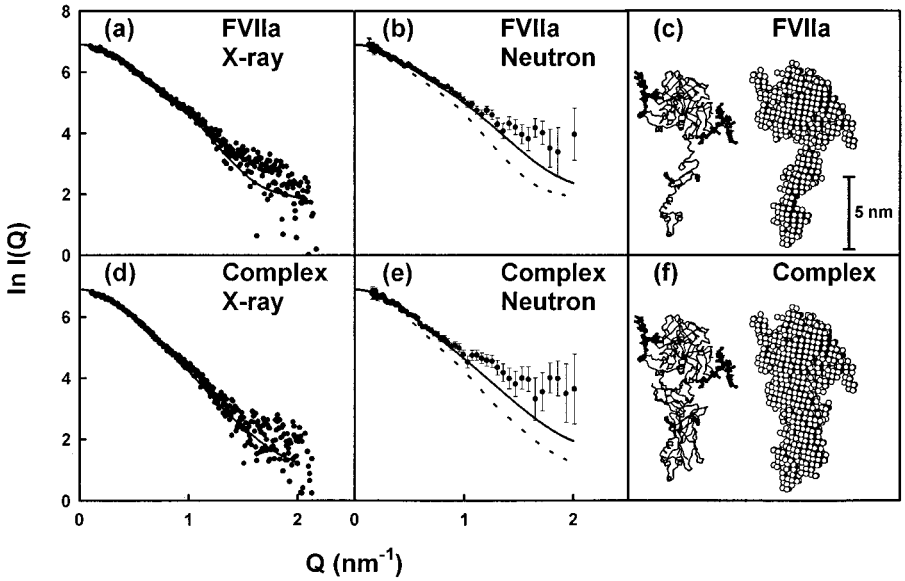

FIGURE 3: Comparison of the calculated and experimental wide-angle scattering curves $I(Q)$ for FVIIa and its complex with sTF. The continuous lines represent the curves calculated from the crystal structure, while the points correspond to experimental data. (a, b): curve fits for the X-ray and neutron data, respectively, based on the FVIIa structure seen in the FVIIa−sTF complex. (c): sphere model and α-carbon views of the FVIIa structure in the FVIIa−sTF complex, in which the full oligosaccharide structures are shown in bold. (d, e): curve fits for the X-ray and neutron data, respectively, based on the FVIIa−sTF crystal structure. (f): α-carbon and sphere model views of the FVIIa−sTF structure in the same orientation as that of (c), in which the FVIIa oligosaccharide structure is shown in bold outline in the former. The dashed lines shown in (b) and (e) correspond to the calculated curves depicted in (a) and (d) to show the effect of the neutron instrumental corrections.

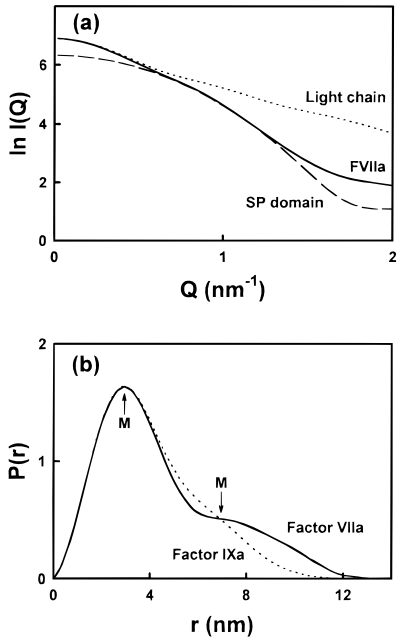

FIGURE 4: Scattering curves calculated from the crystal structures of FVIIa and FIXa. (a): the scattering curves $I(Q)$ calculated from the SP domain and the light chain in the FVIIa model of Figure 3c are compared with the calculated X-ray scattering curve of FVIIa taken from Figure 3a. (b): the distance distribution functions $P(r)$ are shown to correspond to the calculated scattering curves of FVIIa and FIXa, with the position of two peaks indicated by M.

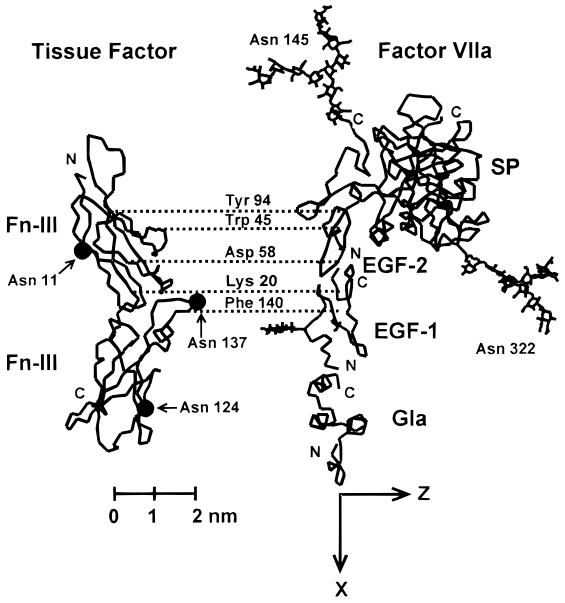

FIGURE 5: α-Carbon trace views of the sTF and FVIIa domain structures. The linear domain structure for FVIIa is the starting model with arbitrary domain orientations that was used for the automated searches. The oligosaccharides at Asn145 and Asn322 are shown in extended conformations, in contrast to the more compact conformations shown in Figure 3. The C-terminal domain of sTF is positioned proximate to the N-terminal Gla domain in FVIIa in the complex. Distance constraints based on the positions of Lys20, Trp45, Asp58, Tyr94, and Phe140 in sTF are indicated by dotted lines that represent the perpendiculars from these α-carbon atoms to the long x axis of the FVIIa model. The mean of the five perpendicular distances is denoted as D in the text. The α-carbon positions of the three N-linked oligosaccharides on sTF are indicated by ● symbols (see text). The x and z axes are as indicated; the y axis is perpendicular to the page.

FVIIa model contained 666 spheres and that for sTF contained 354 spheres.

The X-ray and neutron scattering curves $I(Q)$ were calculated from the sphere models by an application of Debye's Law adapted to spheres of a single density (*22*, *40*). In neutron curve fits, the hydration shell is not detectable and the dry sphere models obtained directly from the grid transformation were used for curve fitting. For X-ray curve fits, a hydration of 0.3 g of H_2O/g of glycoprotein and an electrostricted volume of 0.0245 nm^3/H_2O molecule were

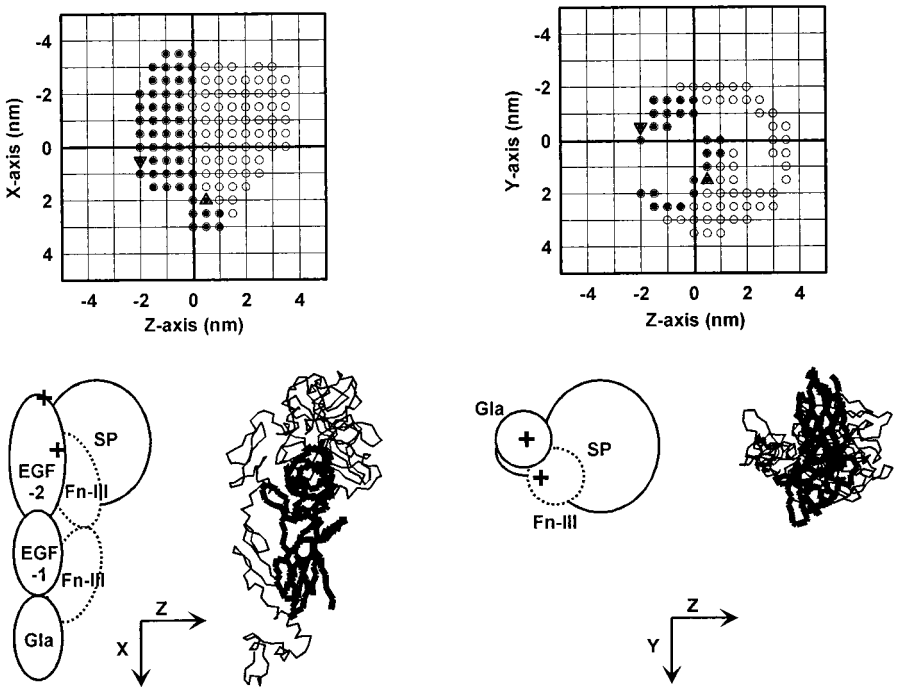

FIGURE 6: Two projection views of the outcome of the automated search for the FVIIa−sTF complex. The *zx* and *zy* projection views summarize the distribution of 276 sTF structures relative to the FVIIa model after the exclusion of models with large steric overlap or large R_G values. The *zx* projection is shown also in Figure 5. Below each grid, outlines of the FVIIa and sTF domains are shown in the same scale to show the best-fit structure for the complex, denoted by the Δ symbol in the grid. The + symbol on FVIIa denotes the origin of the grid, and the + symbol on sTF (dotted outline) denotes its N terminus. Note that the separation between the two + symbols matches the separation of the origin of the grid and the Δ symbol in the grid. The ○ and ● symbols in the grid denote the position of the N terminus of sTF in the 276 models of the complex. ○ denotes 184 complex models with *D* values greater than 2.5 nm, while ● denotes 92 complex models with *D* less than 2.5 nm that satisfy the biochemical constraint of Figure 5 (see text). The ∇ symbol denotes the worst-fit model from the 276 models. Also shown is an α-carbon view of the crystal structure of the FVIIa−sTF complex in the same orientation and scale as the domain outline, with sTF shown in bold.

used to readjust the sphere radius and coordinates to allow for the volume of the hydrated structure (*23*−*25*). For X-ray fits, no scattering curve corrections were applied for wavelength spread or beam divergence as these are thought to be negligible. For neutron fits, a 16% wavelength spread for a nominal λ of 1 nm and a beam divergence of 0.016 rad were used as an empirical correction for the calculated scattering curves (*26*).

The curve fits were assessed by calculating the radius of gyration R_G and that of its cross-section R_{XS} from Guinier fits of the calculated curve in the same *Q* ranges used in the experimental data analyses (*29*). The *R* factor goodness-of-fit parameter was defined by analogy with crystallography (*23*) for X-ray data in the *Q* range between 0.10 and 2.0 nm^{-1} and neutron data in the *Q* range between 0.15 and 2.0 nm^{-1} (denoted as $R_{2.0}$), and normalized using an $I(0)$ value of 1000. Sedimentation coefficients ($s°_{20,w}$ values) were calculated directly from the hydrated sphere models used for X-ray scattering curve fits using the program GENDIA (*24*, *41*, *42*). In the automated searches, the comparison of the calculated and experimental curves was achieved by the use of filters to retain or reject models on the basis of less than 5% steric overlap between the domains, specified ranges for the calculated R_G and R_{XS} values and $s°_{20,w}$ values, and low *R* factor values (*22*). For FVIIa and the complex, the R_G value of their models was required to be less than 3.21 and 3.4 nm, respectively (Table 1).

RESULTS AND DISCUSSION

(a) Comparison of the Solution and Crystal Structures for FVIIa. In the absence of a crystal structure for free FVIIa, the solution scattering data for free FVIIa in 5 mM Ca^{2+} were compared with the FVIIa structure found within the crystal structure of the FVIIa−sTF complex to determine the degree of agreement between them. This FVIIa structure in the sTF−FVIIa crystal complex showed an extended arrangement of the Gla, EGF-1, and EGF-2 domains with a tip-to-tip maximum dimension of 11.5 nm. This is comparable with the length determination of 10.3 nm for FVIIa in solution by scattering (*29*). The FVIIa crystal structure showed that the EGF-2 and SP domains form many contacts with each other and may be considered as a rigid entity, and that the link between the Gla and EGF-1 domains is also well-defined. One less well defined feature is the extended oligopeptide link HKDDQLI between the last disulfide bridge of EGF-1 and the first disulfide bridge of EGF-2 domains (residues 84−90 in Figure 2). This forms a poorly defined helix in the crystal structure that may be flexible in solution (Figure 1). The two large N-linked oligosaccharide chains on opposite faces of the SP domain were not visible in the crystal structure of the complex, and constitute a second less well defined feature of the FVIIa structure. When the scattering curve was calculated for the FVIIa structure seen in the crystal structure of the complex with the addition of two extended oligosaccharide chains (Methods; see Figure 5), R_G and R_{XS} values of 3.46 and 1.43 nm, respectively, were obtained that were higher than the experimental values. The X-ray and neutron curve fits had goodness-of-fit $R_{2.0}$ values of 7.6% and 7.9%, respectively (Table 1a). However, if the oligosaccharide chains were reorientated more closely to the protein surface of the SP domain in this FVIIa

Table 1: Modeling Analyses for Factor VIIa and the Complex between Factor VIIa and Soluble Tissue Factor

	models	R_G (nm)	R_{XS} (nm)	$R_{2.0}$ (%)	$s^\circ_{20,w}$ (S)
(a) Factor VIIa:					
mean experimental values		3.31 ± 0.08	1.53 ± 0.13		3.3 ± 0.1[a]
calculated values using models from crystal structures					
FVIIa from FVIIa−sTF (extended CHO)	1	3.46	1.43	7.0, 7.0[b]	3.0
FVIIa from FVIIa−sTF (compact CHO)	1	3.31	1.55	5.7, 6.0[b]	3.2
FIXa-based (extended CHO)	1	3.21	1.37	6.5, 7.5[b]	3.3
FIXa-based (compact CHO)	1	3.06	1.49	4.8, 6.7[b]	3.5
automated search using homology models ($5 \times 72°$ steps about x, y, z axes)					
linear starting model	1	3.22	1.30	4.4, 6.8[b]	3.4
bent model	1	2.58	1.61	19.3, 14.7[b]	3.8
number of models	15 625				
models with < 5% steric overlap	11 955	2.90 ± 0.19	1.40 ± 0.12	5.4 ± 2.0	3.6 ± 0.12
models with $R_G > 3.15$ nm	1051	3.20 ± 0.03	1.31 ± 0.03	4.4 ± 0.2	3.4 ± 0.03
models with $R_G > 3.21$ nm	317	3.24 ± 0.02	1.32 ± 0.02	4.6 ± 0.2	3.4 ± 0.02
(b) FVIIa−sTF Complex:					
mean experimental values		3.22 ± 0.03	1.56 ± 0.02		4.4 ± 0.3[a]
calculated values using models from crystal structure					
FVIIa−sTF complex (extended CHO)	1	3.57	1.56	8.4, 7.7[b]	4.3
FVIIa−sTF complex (compact CHO)	1	3.47	1.60	6.5, 6.8[b]	4.5
automated search using homology models (21×0.5 nm steps along x, y, z axes; 4 orientations)					
total number of models	4×9261				
orientation 1 (models with <5% steric overlap; $R_G < 3.4$ nm)	276	3.35 ± 0.04	1.72 ± 0.08	6.5 ± 1.2	4.5 ± 0.1
best model	1	3.24	1.64	3.8, 8.3[b]	4.7

[a] Experimentally determined values (Methods). [b] The first and second values correspond to the X-ray and neutron $R_{2.0}$ values, respectively.

structure, R_G and R_{XS} values of 3.31 and 1.55 nm, respectively, were obtained that were in good agreement with the experimental values. The X-ray and neutron $R_{2.0}$ values were better at 5.7% and 6.0%, respectively (Table 1a). It was concluded that a FVIIa structure with an extended EGF-1/EGF-2 link and compact N-linked oligosaccharides (Figure 3c) is consistent with the experimental data for free FVIIa in solution.

As FVIIa is 90% protein and 10% carbohydrate by weight, scattering inhomogeneity effects may be important. The X-ray data correspond to a high positive solute−solvent contrast, while the neutron data in 100% ^2H_2O correspond to a high negative solute−solvent contrast that inverts the relative contributions of high and low macromolecular scattering densities to the observed scattering curve. The similarity of the $R_{2.0}$ values for both the X-ray curve fit (Figure 3a) and the neutron curve fit (Figure 3b) after correction for instrumental effects (see dotted lines in Figure 3b) showed that these inhomogeneity effects were unimportant.

The four domains of FVIIa are homologous to those found in FIXa. In the crystal structure of free porcine FIXa, three of its four domains were clearly visualized. The fourth (Gla) domain was partially resolved but could be successfully modeled using the prothrombin Gla domain structure (*17*). The FIXa crystal structure exhibits a sharp 110° bend between the long axes of the EGF-1 and EGF-2 domains in the light chain that is stabilized by a salt bridge unique to FIXa between Glu78 and Arg97 in the numbering of Figure 2. The oligopeptide linker between EGF-1 and EGF-2 in FIXa is four residues shorter than that seen in FVIIa (Figure 2). The maximum linear dimension of the four FIXa domains is accordingly shorter at 10.5 nm than that of 11.5 nm for FVIIa. To test whether this shorter, bent FIXa domain arrangement could represent the domain structure of free FVIIa in solution, a scattering curve was calculated from this FIXa crystal structure (Methods) for comparison with the experimental FVIIa scattering data. If extended oligosaccharide structures were used in this model, the resulting R_G and R_{XS} values of 3.21 and 1.37 nm, respectively, were close to the experimental values, and X-ray and neutron $R_{2.0}$ values of 6.5% and 7.5%, respectively, were obtained (Table 1a). When compact oligosaccharide structures were used, the resulting R_G value of 3.06 nm was in poorer agreement with the experimental value, but better $R_{2.0}$ values of 4.8% and 6.7% were obtained. The inconsistency of these two outcomes, together with visual inspection of the two curve fits (not shown), did not favor a bent FIXa-like domain arrangement as a model for the FVIIa domain arrangement in solution (Table 1a).

Comparative calculations of the scattering curve $I(Q)$ and its distance distribution function $P(r)$ from the crystal structures of complexed FVIIa and free FIXa (Figure 4) showed more clearly that FVIIa in solution contains an extended light chain domain arrangement and not a bent one. The experimental X-ray $I(Q)$ for free FVIIa in Figure 3a showed a slight inflection at $Q = 0.9$ nm^{-1}, which suggested that structurally distinct and separated "head" and "tail" moieties existed in free FVIIa. Even though the whole FVIIa structure contributes to all parts of the FVIIa $I(Q)$ curve, the calculation of $I(Q)$ for the SP domain alone gave a good match to the FVIIa curve between Q of 0.6−1.3 nm^{-1} in Figure 4a, while that for the light chain alone in FVIIa gave a good match to the FVIIa curve below Q of 0.35 nm^{-1} in the Q range where the SP curve is relatively flat in Figure 4a. This provided an explanation of the inflection in $I(Q)$ at $Q = 0.9$ nm^{-1}. Similar calculations using the FIXa crystal structure gave neither of these matches (not shown), which is attributable to the closer spatial proximity of the SP domain to the light chain in this bent structure. More significantly, the $P(r)$ curves from the crystal structures of complexed FVIIa and free FIXa showed a large difference (Figure 4b). That for FVIIa contains a main peak at M of 3.0 nm and a subpeak at 7.0 nm. That at 3.0 nm is assigned to interatomic

distances mostly within the SP domain, while that at 7.0 nm is assigned to interatomic distances mostly within an extended light chain structure, the second of which has 31% of the height of the main peak. The calculated curve was in excellent agreement with the experimental $P(r)$ curve of free FVIIa which shows two peaks at 3.0 and 7.0 nm, the second of which has a peak height of 32% of the first (see Figure 3 in ref *29*). In contrast, the $P(r)$ curve for FIXa contained only a main peak at 3.0 nm (Figure 4b). This is attributable to the proximity of the SP domain and light chain in the bent FIXa structure. Thus, the difference between the two $P(r)$ curves rules out a significantly bent light chain domain structure for free FVIIa in solution.

(b) Automated Modeling Curve Fitting for the FVIIa Domains. Solution scattering does not yield unique structures but only compatible ones. Since the above results for FVIIa were based on comparisons with only two crystal structures, supplementary curve fits were needed in order to establish a more general structural description for FVIIa. Thus an automated curve fit analysis was performed to assess all possible domain arrangements (Methods). A linear starting model that corresponded to the most extended domain arrangement positioned the long axes of the Gla, EGF-1, and EGF-2 domains on a common long axis included a short linker between the EGF-1 and EGF-2 domains and possessed extended oligosaccharide structures. Since the FVIIa−sTF crystal structure was unavailable at the time the search was performed, this starting model was constructed from homologous domains found in prothrombin, FIXa, and factor Xa (Methods; Figure 5). This model had a length of 11.0 nm and gave an acceptable curve fit to the experimental X-ray data. The R_G and R_{XS} values were low at 3.22 and 1.30 nm, but good X-ray and neutron goodness-of-fit $R_{2.0}$ values of 4.4% and 6.8% were obtained. In contrast, a bent domain model in which the EGF-1 and Gla domains were both rotated by 72° about the y axis in the $x-z$ plane of Figure 5 gave very poor curve fits with $R_{2.0}$ values of 19.3% and 14.7%.

This linear starting FVIIa model was used for an automated curve-fit search based on 15 625 possible domain arrangements, which were evaluated using fits to the experimental X-ray curve. The application of a steric overlap filter left 11 955 models (Methods; Table 1a). Of these models, only 1051 had R_G values greater than 3.15 nm, and 317 had R_G values greater than 3.21 nm. These 317 models (which included the starting linear model) had individual x-, y-, and z-axis rotations that were distributed over all values without preference for specific ranges, and gave good agreement with the experimental X-ray data. In conclusion, the search showed that only the most extended domain arrangements in free FVIIa were compatible with the experimental X-ray curve. These correspond not only to the extended FVIIa structure seen in the FVIIa−sTF crystal structure, but also to other structures that may be in equilibrium with this, provided that all these other structures are extended. In addition, this search did not rule out the presence of a short linker structure between EGF-1 and EGF-2 in free FVIIa, which becomes more elongated after complexation with sTF to give the FVIIa structure seen in the FVIIa−sTF complex.

(c) Comparison of the Crystal and Solution Structures for the FVIIa−sTF Complex. To see whether the crystal structure of inhibited FVIIa and subtilisin-cleaved sTF (*14*) is compatible with the solution structure of the FVIIa−sTF complex, the scattering curve calculated from the crystal structure was compared with the experimental scattering curves for the complex formed between intact sTF and inhibited FVIIa in Figure 3, parts d and e. The same extended and compact N-linked oligosaccharide structures used above for free FVIIa were used in order to permit direct comparison with the FVIIa curve fits. Small curve fit differences for the complex were seen between the two oligosaccharide conformations, and the compact one again gave a better curve fit (Figure 3f). The experimental R_G values of free FVIIa and the FVIIa−sTF complex are similar within experimental error (Table 1), and this was attributed to the compact nature of the interaction made between FVIIa and sTF in their complex (*29*). In the present modeling, the calculated R_G value for the complex was larger by 0.25 nm than the experimental value; however, satisfactory X-ray and neutron $R_{2.0}$ values of 6.5−6.8% were obtained, and this supported the similarity of the crystal and solution structures of the complex (Table 1b). The difference in R_G values may be attributed to the less extensive data collection for the complex compared to FVIIa in ref 29. It was concluded that the curve fits of Figure 3d, e ruled out the possibility of a major domain rearrangement between the crystal and solution states.

(d) Automated Modeling Curve Fitting for the FVIIa−sTF Complex. The feasibility of an automated curve-fit search to determine candidate models for a multidomain heterodimeric protein complex is important for the study of other such systems. This was therefore examined using the FVIIa−sTF complex as a model system, since these candidate models can be compared with the recently solved crystal structure for this complex. Such a search assumes that major structural rearrangements in the two associating multidomain structures between the free and bound states are absent. For sTF, supporting evidence for this was obtained by the comparison of scattering curves calculated for free and complexed sTF crystal structures (Methods), which gave good $R_{2.0}$ values of 2.3−3.5%. Comparisons of the calculated R_G values of 2.34−2.49 nm with the experimental value of 2.06 ± 0.12 nm (*29*) showed that these were larger by 0.28−0.43 nm. This R_G difference is attributed to the small size of sTF and the less extensive data collection for sTF compared to FVIIa in the earlier study (*29*), and is not considered significant in the present context. For FVIIa, only extended domain arrangements in the free and complexed forms were determined from the above analyses, and the extended linear FVIIa structure of Figure 5 was therefore reused here.

A comprehensive search for all sterically allowed structures of sTF relative to FVIIa in the complex would involve six rotational and translational parameters. Their full treatment would result in too many models to analyze with present computational resources. Previously, automated curve-fit searches for two homooligomeric complexes were constrained by symmetry and this significantly reduced the number of models to be tested (*22*, *25*, *31*). As symmetry constraints were not available for a heterodimeric complex, a biochemical constraint was used instead. It is known that the C-terminal domain of sTF is close to the Gla domain of FVIIa, since the EGF-1 and Gla domains interact with sTF (*43*), and both the C-terminal domain of sTF and the Ca^{2+}-

rich Gla domain are proximal to the negatively charged cell membrane in the membrane-bound complex. This constraint fixed the position of sTF so that the C-terminus of sTF was close to the Gla domain (shown in Figures 1 and 5). Accordingly only translational searches of sTF in this orientation relative to FVIIa were performed and this restricted the number of models to be tested to 9261 (Methods). Three further searches were also made with the sTF structure rotated in 90° steps about its longest axis (Methods).

Analysis of the conformational searches identified 276 possible structures for the complex in the search based on the sTF orientation shown in Figure 5, where 97% of the 9261 possible models had been eliminated by the use of steric overlap and R_G filters. The two filters eliminated models that were too compact or too elongated, respectively. The 276 structures included those related to the known crystal structure of the complex. At this point, further biochemical constraints were found to be useful. This is detailed as follows:

(i) Projection views of these 276 models (Figure 6) showed that a sufficiently large translational range had been scanned. Both the R_G and R_{XS} values of the 276 models agreed with experiment and gave low $R_{2.0}$ values between 3.8% and 9.4%. Similar results were obtained in the other three searches using the different sTF orientations about its long axis (not shown). The 276 locations of sTF relative to FVIIa in the *zx* (and *yx*) projection covered a large area on the longest *x* axis of FVIIa. The *zy* projection shows that the 276 locations correspond to an annulus that surrounds the three small Gla and EGF domains or the large SP domain. Analysis of all four 90° orientations of sTF about its longest axis (not shown) showed that the greatest uncertainty in the position of these filtered models was along the *x*-axis (range of 5 nm), followed by the *z*-axis (range of 4 nm), then the *y*-axis translation (range of 2 nm).

(ii) Surface plasmon resonance analyses of mutants have shown that the sTF residues Lys20, Trp45, Asp58, Tyr94, and Phe140 (Figure 5) are important for binding to the Gla and EGF domains in FVIIa (*2, 3*). The biochemical constraint based on this was used to divide the 276 models into two sets. The mean value *D* of the perpendicular distances between these five α-carbon atoms in sTF and the *x* axis of FVIIa (Figure 5) was 3.0 ± 1.1 nm for all 276 models. The 92 models with *D* less than 2.5 nm (highlighted as ● in Figure 6) correspond to an annulus of sTF locations surrounding the Gla and EGF domains in the *zy* projection. The *zx* projection showed that the 92 highlighted locations covered the long axis of the EGF and Gla domains.

(iii) The best X-ray fit model (Δ) had *x*, *y*, and *z* translations of sTF by 2.0, 1.5, and 0.5 nm, respectively, from the origin, with a separation between the centers of mass of 2.6 nm (Table 1b; Figure 6), and gave an $R_{2.0}$ value of 3.8%. This model and others were located in the $+z/+y$ quadrant in the *zy* projection. This quadrant corresponds to the large space contained between the SP domain and the light chain. Comparison of the domain outlines in Figure 6 with molecular graphic views of the crystal structure of the complex provided a striking confirmation of the layout of FVIIa and sTF in this best-fit structure (Figure 6). The rotational orientations of the FVIIa domains and sTF about their long axes were, however, distinctly different in the crystal structure compared to Figure 5 and could not be identified in this search. The worst X-ray fit model (∇) and others were located in the $-z/-y$ quadrant in the *zy* projection, in which sTF is now on the opposite face of FVIIa.

(iv) Two final checks were performed on the best-fit model from the search (Figure 6). The occupancy of the three Asn glycosylation sites in native tissue factor would hinder protein−protein interactions with FVIIa, and their location acts as a biochemical constraint that defined disallowed models. In Figure 5, Asn124 and Asn137 are on the right side of sTF, while Asn11 is on the left, and define possible surface areas of sTF that do not interact with FVIIa. This was sterically consistent with the best-fit model from the search shown in Figure 5. This best-fit model was supported also by the 276 corresponding neutron curve fits, where the best model had $R_{2.0} = 8.3\%$ and the worst one had $R_{2.0} = 10.3\%$.

(e) Sedimentation Coefficient Analyses for FVIIa and Its Complex with sTF. The modeling of sedimentation coefficient data from analytical ultracentrifugation provides an alternative determination of the dimensions of FVIIa and the FVIIa−sTF complex. Previously, using models based on hydrodynamic ellipsoids, the Perrin equations resulted in molecular dimensions for FVIIa of 20.4 nm × 2.8 nm × 2.8 nm at one limit and 12.6 nm × 9.8 nm × 1.4 nm at the other (*44, 45*). Those for the FVIIa−sTF complex were 25.4 nm × 2.6 nm × 2.6 nm at one limit and 18.6 nm × 7.8 nm × 1.2 nm at the other. Since X-ray and neutron scattering showed that both FVIIa and the FVIIa−sTF complex had lengths of 10.2−10.3 nm, and the crystal structure for the FVIIa−sTF complex is 11.5 nm long with a diameter of 4.0−5.0 nm, the lengths from scattering are seen to be in better agreement with the FVIIa−sTF crystal structure than those from the Perrin equations. This discrepancy is now explored.

Hydrodynamic modeling was performed to assess the use of sedimentation coefficients $s^\circ_{20,w}$ to analyze these structures. First, remeasurement of the experimental $s^\circ_{20,w}$ values for FVIIa and the FVIIa−sTF complex gave values of 3.3 ± 0.1 S and 4.4 ± 0.3 S, respectively, from sedimentation velocity runs using a Beckman XLA ultracentrifuge (Methods). While the first value is in good agreement with that of 3.4 ± 0.1 S reported previously using a Beckman Model E ultracentrifuge (*44*), the second value is higher than that of 3.9 ± 0.1 S determined previously. Second, using small spheres, the theoretical $s^\circ_{20,w}$ values were calculated from the crystallographic models and the automated search models for comparison with experiment (Table 1). In agreement with the scattering modeling, the $s^\circ_{20,w}$ calculation for the FVIIa model derived from the crystal structure of the complex was in better agreement with experiment if the oligosaccharides were in a compact conformation (Table 1a). Likewise the 317 best-fit FVIIa scattering models from the automated search gave good agreement with experiment (Table 1a). These showed that the use of small spheres was successful in accounting for the experimental $s^\circ_{20,w}$ value of 3.3 ± 0.1 S. However, unlike the scattering analyses, the $s^\circ_{20,w}$ calculation could not exclude the bent FVIIa model derived from FIXa (Table 1a). In the case of the FVIIa−sTF complex, good agreement was also found with the crystal structure which gave calculated $s^\circ_{20,w}$ values of 4.3−4.5 S in good agreement with the experimental value of 4.4

± 0.3 S (Table 1b). The 276 best-fit scattering models gave a calculated mean value of 4.5 ± 0.1 S. It is concluded that the scattering and hydrodynamic calculations were consistent with each other, and that the earlier measurement of $s^{\circ}_{20,w}$ for the complex had been underestimated.

CONCLUSIONS

(a) Structures of FVIIa and FVIIa−sTF. Solution scattering has provided new information on the domain arrangements in FVIIa and the FVIIa−sTF complex that usefully extends the interpretation of recent crystal structures for coagulation factors, both when free and when complexed. Multidomain structures cannot be solved unambiguously by scattering analyses, but the knowledge of these crystal structures now places limits on the scattering analyses and makes them more powerful in the analysis of unknown multidomain structures (*22*).

In application to FVIIa, previous scattering studies had indicated that the FVIIa domains were extended (*29*). Here, the direct comparison of scattering data for free FVIIa in solution with the extended FVIIa structure in the recent crystal structure of the FVIIa−sTF complex shows that they are consistent. In addition, several new curve-fit analyses rule out a bent light chain structure for FVIIa such as seen in the crystal structure of the homologous coagulation factor FIXa. In FIXa, the bend in this structure occurs at the short EGF-1/EGF-2 link and is attributed to a Glu-Arg interdomain salt bridge that is conserved in FIXa but not in either FVIIa or factor Xa. In FVIIa, this link is longer and is seen as a short poorly formed helix in the FVIIa−sTF crystal structure to suggest that this may be somewhat flexible and extended in solution, which would be consistent with the new curve fits presented here. Fluorescence experiments with labeled FVIIa have suggested that free FVIIa is more flexible than in the complex with sTF (*44*). This link is also likely to be flexible in factor Xa as this link is longer than that of FIXa, and EGF-2 but not EGF-1 was observed in the crystal structure of des-Gla factor Xa (*15*). In a second crystal form of des-Gla factor Xa, the EGF-1 domain is in a different location relative to the SP and EGF-2 domains (*16*). In addition, the NMR structure of the Gla/EGF-1 domain pair in factor X suggests that there is flexibility between these two domains as well (*46*). These observations imply that multiple related FVIIa conformations of similar energies may coexist in solution. The significance of the present automated FVIIa curve-fit analyses is to show that all these extended structures will be similar in overall length and ideal for the recognition of tissue factor. There would be no significant energy price to be paid in terms of domain reorientation during complex formation, and this together with the extensive dispersion of contact residues across the four FVIIa domains would account for the low nanomolar K_D reported for the interaction.

In application to the FVIIa−sTF complex, the scattering data showed that a compact complex of FVIIa with sTF was formed (*29*). The present scattering analysis was important to verify the similarity of its domain structure in solution with that in the crystal structure, despite the removal of the sTF residues 85−89 in the crystal structure and the existence of packing contacts in the crystal state. It is generally thought that the tight interaction of the Gla, EGF-1, EGF-2, and SP domains in FVIIa with the domain pair in sTF locks the flexible FVIIa structure into a more rigid conformation. This would stabilize an active conformation and/or a reorientation of the enzymatic SP domain in FVIIa that would lead to its activation and the initiation of blood coagulation (*3*, *30*). Data from a fluorescence energy transfer study suggest that this may well be the case (*47*). A crystal structure for free FVIIa would therefore be of great interest as this would allow the precise definition of changes in the SP domain in relation to FVIIa function.

Solution scattering also provided information on the two N-linked oligosaccharide structures of FVIIa. Since these lie on the outer periphery of FVIIa, scattering data are sensitive to their conformation. The FVIIa curve fits suggest that these oligosaccharides are not as extended as found in several other glycoproteins by similar scattering analyses (*25*, *28*), and the same result was obtained with the FVIIa−sTF curve fits. Their conformations shown in Figures 3c and 5 suggest that two sides of the SP domain are masked, while leaving accessible the catalytic triad at His193-Asp242-Ser344 at the top of the structure as viewed in Figure 3f, as well as its contact region with sTF between the SP domain and the FVIIa light chain. The O-linked oligosaccharides on the EGF-1 domain likewise do not mask the contact surface of FVIIa. Inspection of the sTF structure in its complex shows that the N-linked oligosaccharides of sTF also do not hinder the contact region of sTF with FVIIa.

(b) Automated Modeling of Heterodimeric Complexes by Scattering and Ultracentrifugation. The novelty of the present curve-fit modeling lies in its application to a heterodimeric complex formed between two multidomain proteins (*22*). The joint use of both X-ray and neutron scattering curve fits together with analytical ultracentrifugation data serves as controls for reproducibility and possible solute−solvent contrast effects. Previous curve-fit applications have described its calibration for proteins of known crystal structures and molecular weights between 23 000 and 127 000 (*23*−*25*) and its application to single multidomain proteins and homodimeric and homotrimeric complexes (*26*−*29*). In the present application, as in those previous ones, suitable homologous atomic structures are essential to constrain the curve-fit analyses. These may be available either directly by high sequence similarity with known atomic structures (homology modeling) or indirectly by protein fold recognition methods and analogy modeling (*48*, *49*). For single multidomain proteins, further constraints are imposed by use of the correct stereochemical connections between the domains that the curve fits are directed toward determination of the domain arrangement. For homooligomeric complexes, further constraints are imposed through known symmetry relationships that the curve fits can assess the arrangement of the monomers within the oligomer. The present analysis of a heterodimeric complex, however, lacks symmetry constraints. After constraining the search on the basis of the inferred relative orientation of the two proteins in the complex, the use of steric overlap and R_G filters still left many allowed structures. However, in the search based in Figure 5, the use of further biochemical constraints based on identified contact residues between the two proteins (together with the known location of glycosylation sites which would be excluded from the protein−protein interface) permitted the location of sTF in the space between the SP

domain and the light chain, in agreement with the crystal structure of the complex. This approach usefully narrowed the range of possible structures for the complex. Thus, in the absence of a crystal structure, it is envisaged that the automated modeling technique with the application of biochemical constraints, together with the use of electrostatic and surface docking methods, will result in improvements in structure determinations for other heterodimeric complexes such as ligand−receptor pairs.

ACKNOWLEDGMENT

A.W.A. and S.J.P. thank the Biotechnology and Biological Sciences Research Council for grant support. G.K.C. and D.J.D.J. are supported by the Medical Research Council. We thank Prof. E. G. D. Tuddenham for his interest and support, Dr. D. M. A. Martin for useful discussions, Dr. A. J. Rowe (Leicester) for hydrodynamic measurements, and Dr. D. W. Banner (Hoffman-La Roche) for the prerelease of the FVIIa−sTF coordinates.

REFERENCES

1. O'Brien, D. P., Kemball-Cook, G., Hutchinson, A. M., Martin, D. M. A., Johnson, D. J. D., Byfield, P. G. H., Takamiya, O., Tuddenham, E. G. D., and McVey, J. H. (1994) *Biochemistry 33*, 14162−14169.
2. Kelley, R. F., Costas, K. E., O'Connell, M. P., and Lazarus, R. A. (1995) *Biochemistry 34*, 10383−10392.
3. Martin, D. M. A., Boys, C. W. G., and Ruf, W. (1995) *FASEB J. 9*, 852−859.
4. Morrissey, J. H., Neuenschwander, P. F., Huang, Q., McCallum, C. D., Su, B., and Johnson, A. E. (1997) *Thromb. Haemostasis 78*, 112−116.
5. Edgington, T. S., Dickinson, C. D., and Ruf, W. (1997) *Thromb. Haemostasis 78*, 401−405.
6. Banner, D. W. (1997) *Thromb. Haemostasis 78*, 512−516.
7. Østerud, B. (1997) *Thromb. Haemostasis 78*, 755−758.
8. Semeraro, N., and Colucci, M. (1997) *Thromb. Haemostasis 78*, 759−764.
9. Harlos, K., Martin, D. M. A., O'Brien, D. P., Jones, E. Y., Stuart, D. I., Polikarpov, I., Miller, A., Tuddenham, E. G. D., and Boys, C. W. G. (1994) *Nature (London) 370*, 662−666.
10. Muller, Y. A., Ultsch, M. H., Kelley, R. F., and De Vos, A. M. (1994) *Biochemistry 33*, 10864−10870.
11. Muller, Y. A., Ultsch, M. H., and De Vos, A. M. (1996) *J. Mol. Biol. 256*, 144−159.
12. Williams, A. F., and Barclay, A. N. (1988) *Annu. Rev. Immunol. 6*, 381−405.
13. Bork, P., Holm, L., and Sander, C. (1994) *J. Mol. Biol. 242*, 309−320.
14. Banner, D. W., D'Arcy, A., Chene, C., Winkler, F. D., Guha, A., Konigsberg, W. H., Nemerson, Y., and Kirchofer, D. (1996) *Nature (London) 380*, 41−46.
15. Padmanabhan, K., Padmanabhan, K. P., Tulinsky, A., Park, C. H., Bode, W., Huber, R., Blankenship, D. T., Cardin, A. D., and Kisiel, W. (1993) *J. Mol. Biol. 232*, 947−966.
16. Brandstetter, H., Kühne, A., Bode, W., Huber, R., von der Saal, W., Wirthensohn, K., and Engh, R. A. (1996) *J. Biol. Chem. 271*, 29988−29992.
17. Brandstetter, H., Bauer, M., Huber, R., Lollar, P., and Bode, W. (1995) *Proc. Natl. Acad. Sci. U.S.A. 92*, 9796−9800.
18. Selander, M., Persson, E., Stenflo, J., and Drakenberg, T. (1990) *Biochemistry 29*, 8111−8118.
19. Baron, M., Norman, D. G., Harvey, T. S., Handford, P. A., Mayhew, M., Tse, A. G. D., Brownlee, G. G., and Campbell, I. D. (1992) *Protein Sci. 1*, 81−90.
20. Soriano-Garcia, M., Padmanabhan, K., De Vos, A. M., and Tulinsky, A. (1992) *Biochemistry 31*, 2554−2566.
21. Perkins, S. J. (1994) Physical Methods of Analysis, in *Methods in Molecular Biology* (Jones, C., Mulloy, B., and Thomas, A. H., Eds.) Vol. 22, 39−60, Humana Press Inc., New Jersey.
22. Perkins, S. J., Ashton, A. W., Boehm, M. K., and Chamberlain, D. (1998) *Int. J. Biol. Macromol. 22*, 1−16.
23. Smith, K. F., Harrison, R. A., and Perkins, S. J. (1990) *Biochem. J. 267*, 203−212.
24. Perkins, S. J., Smith, K. F., Kilpatrick, J. M., Volanakis, J. E., and Sim, R. B. (1993) *Biochem. J. 295*, 87−99.
25. Ashton, A. W., Boehm, M. K., Gallimore, J. R., Pepys, M. B., and Perkins, S. J. (1997) *J. Mol. Biol. 272*, 408−422.
26. Mayans, M. O., Coadwell, W. J., Beale, D., Symons, D. B. A., and Perkins, S. J. (1995) *Biochem. J. 311*, 283−291.
27. Beavil, A. J., Young, R. J., Sutton, B. J., and Perkins, S. J. (1995) *Biochemistry 34*, 14449−14461.
28. Boehm, M. K., Mayans, M. O., Thornton, J. D., Begent, R. H. J., Keep, P. A., and Perkins, S. J. (1996) *J. Mol. Biol. 259*, 718−736.
29. Ashton, A. W., Kemball-Cook, G., Johnson, D. J. D., Martin, D. M. A., O'Brien, D. P., Tuddenham, E. G. D., and Perkins, S. J. (1995) *FEBS Lett. 374*, 141−146.
30. Bazan, J. F. (1996) *Nature (London) 380*, 21−22.
31. Chamberlain, D., O'Hara, B. P., Wilson, S. A., Pearl, L. H., and Perkins, S. J. (1997) *Biochemistry 36*, 8020−8029.
32. Hagen, F. S., Gray, C. L., O'Hara, P., Grant, F. J., Saari, G. C., Woodbury, R. G., Hart, C. E., Insley, M., Kisiel, W., and Kurachi, K. (1986) *Proc. Natl. Acad. Sci. U.S.A. 83*, 2412−2416.
33. Thim, L., Bjoern, S., Christensen, M., Nicolaisen, E. M., Lund-Hansen, T., Pedersen, A. H., and Hedner, U. (1988) *Biochemistry 27*, 7785−7793.
34. Deisenhofer, J. (1981) *Biochemistry 20*, 2361−2370.
35. Bjoern, S., Foster, D. C., Thim, L., Wiberg, F. C., Christensen, M., Komiyama, Y., Pedersen, A. H., and Kisiel, W. (1991) *J. Biol. Chem. 266*, 11051−11057.
36. Harris, R. J., and Spellman, M. W. (1993) *Glycobiology 3*, 219−224.
37. Boys, C. W. G., Miller, A., Harlos, K., Martin, D. M. A., Tuddenham, E. G. D., and O'Brien, D. P. (1993) *J. Mol. Biol. 234*, 1263−1265.
38. Ralston, G. (1993) *Introduction to Analytical Ultracentrifugation*, Beckman Instruments Inc., Fullerton, CA.
39. Perkins, S. J. (1986) *Eur. J. Biochem. 157*, 169−180.
40. Perkins, S. J., and Weiss, H. (1983) *J. Mol. Biol. 168*, 847−866.
41. Garcia de la Torre, J., and Bloomfield, V. A. (1977) *Biopolymers 16*, 1747−1761.
42. Garcia de la Torre, J., and Bloomfield, V. A. (1977) *Biopolymers 16*, 1779−1793.
43. Kazama, Y., Pastuszin, A., Wildgoose, P., Hamamoto, T., and Kisiel, W. (1993) *J. Biol. Chem. 268*, 16231−16240.
44. Waxman, E., Laws, W. R., Laue, T. M., Nemerson, Y., and Ross, J. B. A. (1993) *Biochemistry* 32, 3005−3012.
45. Perrin, F. (1934) *J. Phys. Radium, Ser. VII V*, 497−511.
46. Sunnerhagen, M., Forsén, S., Hoffrén, A.-M., Drakenberg, T., Teleman, O., and Stenflo, J. (1995) *Nat. Struct. 2*, 505−509.
47. McCallum, C. D., Hapak, R. C., Neuenschwander, P. F., Morrissey, J. H., and Johnson, A. E. (1996) *J. Biol. Chem. 271*, 28168−28175.
48. Bazan, J. F. (1990) *Proc. Natl. Acad. Sci. U.S.A. 87*, 6934−6938.
49. Edwards, Y. J. K., and Perkins, S. J. (1996) *J. Mol. Biol. 260*, 277−285.

BI972574V